

Near-far IR photoconductivity damping in hyperdoped Si at low temperatures

SERGEY KUDRYASHOV,¹ KIRILL BOLDYREV,^{2,*} ALENA NASTULYAVICHUS,¹ DMITRY PRIKHOD'KO,^{3,4} SERGEY TARELKIN,^{3,5} DEMID KIRILENKO,⁶ PAVEL BRUNKOV,⁶ ALEXANDER SHAKHMIN,⁷ KAMIL KHAMIDULLIN,^{1,8} GEORGE KRASIN,^{9,*} AND MICHAEL KOVALEV^{1,9}

¹*Lebedev Physical Institute, 119991 Moscow, Russia*

²*Institute of spectroscopy, 108840 Troitsk, Moscow, Russia*

³*Technological Institute for Superhard and Novel Carbon Materials, 108840 Troitsk, Moscow, Russia*

⁴*Moscow Institute of Physics and Technology, Dolgoprudny, 141701 Moscow, Russia*

⁵*The All-Russian Research Institute for Optical and Physical Measurements, 119361 Moscow, Russia*

⁶*Ioffe Institute, 194021 St.-Petersburg, Russia*

⁷*Peter the Great Politechnical University, 195251 St.-Petersburg, Russia*

⁸*ORION research and production enterprise, 111538 Moscow, Russia*

⁹*Bauman Moscow State Technical University, 105005 Moscow, Russia*

*krasin.georg@gmail.com

Abstract: Silicon p-n junction photoelement fabricated on a *p*-doped wafer by sulfur-based *n*-doping of its sub-micron thick surface layer, exhibits at liquid-helium temperatures impurity-based near-far IR (2–21 μm) photoconductivity spectra in the form of well-resolved separate bands of neutral and ionized atomic-like and cluster-like sulfur centers. Temperature variation in the range of 5–105 K demonstrates first at lower temperatures < 35 K strong damping of IR photoconductivity related to cluster-like sulfur centers with ultralow activation energy ≈ 4 meV, corresponding to excitation of the lowest energy of Raman-active phonon in orthorhombic crystalline sulfur lattice. Further increase in temperature results in the next damping step above 85 K for all spectral bands above 1800 cm^{-1} with higher activation energy ≈ 20 meV, representing the lowest energy of Raman-active vibration of octagon molecules in the crystalline sulfur. Broad near-far IR photosensitivity of the hyperdoped material, provided by the concentration-driven sulfur aggregation and quantum-level temperature control of its photoconductivity, paves the way for silicon photonics in far-IR and, possibly in future, even THz spectral regions.

© 2021 Optical Society of America under the terms of the [OSA Open Access Publishing Agreement](#)

1. Introduction

Influence of THz and mid-far IR radiation, probing charge, structural and mesoscopic states of matter, on functional materials, electrical circuits and living organisms is still remaining rather uncovered, partially, because of historical challenges in detection and visualization of transmitted, reflected and scattered radiation in this spectral range [1, 2] (Reststrahlen region [3]). Highly demanded availability of cheap, robust and sensitive photodetectors in this range, potentially, based on advanced silicon (Si) photonics [4, 5], could lead to remarkable breakthroughs in our novel perception of the surrounding world.

Crystalline intrinsic Si, being very abundant, rather cheap and highly transparent material in the range of 1-1000 micrometers [6], appears as a primary candidate material platform of IR and THz photonics, comparing to germanium and III-V and II-VI compounds. Si doping by different impurities [7, 8], introducing shallow and deep optical centers, allows to modify its IR absorption. However, to ensure high IR-photosensitivity, such doping should be high ($>10^{20}$

46 impurity atoms/cm³, hyperdoping) [9, 10]. Such hyperdoping is challenging, since high relative
47 content of impurity atoms perturbs the Si crystalline lattice, leading to local amorphization and
48 degradation of optical and electrical performance [11–13], and requiring ultrashort-pulse laser
49 hyperdoping and subsequent annealing to quench hyperdoped Si states with tremendous non-
50 equilibrium solubility of impurities [14–17]. Importantly, it is high intermediate concentration of
51 impurity that drives its aggregation in Si and related mid-IR broadband absorption, with stronger
52 aggregation providing absorption deeper in IR region. However, ultimate spectral limits for
53 photosensitivity extension into IR region for hyperdoped Si were not explored yet and advanced
54 IR-sensitive Si photo-elements were demonstrated only in the range below 2 micrometers [18–24],
55 comparing to the demonstrated IR-absorption range up to 10 micrometers [9–13, 17]. Hence,
56 comprehensive near-far IR photoconductivity (PC) studies of p-n junctions based on as-fabricated
57 hyperdoped – either annealed, or non-annealed – Si could be crucial differential intermediate
58 tests of both their IR-sensitivity and related electrical performance prior potential harnessing in
59 optoelectronic integration [16–24]. Strong liquid-helium cooling of the hyperdoped samples
60 is required in this case to obtain mid-far IR ($\lambda \approx 2\text{--}20\ \mu\text{m}$) spectra of shallow impurity centers
61 ($E \approx 50\text{--}400\ \text{meV}$) [25–27], while avoiding their considerable bleaching via thermal ionization at
62 $kT \sim E$ and photoconductivity damping via electron-phonon scattering at $kT \sim \hbar\Omega$ (freezing of
63 low-energy phonons with frequencies Ω).

64 2. Materials, procedures and methods

65 In this work, the functional IR-sensitive p-n junction photoelement was fabricated by femtosecond-
66 laser induced n-type sulfur-hyperdoping [17, 28, 29] a submicron-thick surface layer of a p-doped
67 ($\sim 10^{15}\ \text{B-atoms/cm}^3$, specific resistivity $\approx 20\ \Omega\cdot\text{cm}$) 0.38-mm thick commercial Si(111) wafer
68 substrate, irradiated in a raster-scan manner (100 lines/mm, 1 m/s) in liquid carbon disulfide CS₂
69 medium in a glass beaker by 1030-nm, 300-fs 7- μJ pulses, coming at the 100-kHz repetition rate
70 and focused onto the sample surface (the peak surface laser fluence $\approx 1\ \text{J/cm}^2$), as described
71 elsewhere [30]. Its subsequent annealing, similarly to [14], was performed in a muffle oven in
72 ambient air at the temperature of 1150 °C during 30 minutes and quasi-static quenching directly
73 inside the turned off, closed oven accompanied by 10'-ultrasonic cleaning to delaminate the
74 surface oxide layer, according to the procedure described elsewhere [29].

75 Scanning electron microscopy (SEM) visualization of the ablated surface topographies was
76 performed using a microscope TESCAN VEGA, equipped by an energy-dispersion x-ray (EDX)
77 spectrometer, for preliminary in-depth chemical micro-analysis by varying the kinetic electron
78 energy in the incident beam in the range of 4–30 keV. Chemical bonding of silicon, sulfur and
79 carbon atoms across a 1-mm wide of the modified surface layer was studied by means of x-ray
80 photoelectron spectroscopy (XPS). The photoelectron spectra were acquired with Mg-K α line of
81 an analytical module, including a XPS spectrometer with an electron energy analyzer, providing
82 the energy accuracy of 0.1 eV and composition accuracy of 0.15 at. % (84.00-eV Au 4a7/2 line
83 as the standard). According to our EDX characterization, the resulting n-doped layer contained
84 about 0.4 at. % of sulfur, which was distributed, besides the surface oxidized sulfite/sulfate forms
85 (60–70 at. %), in the dissolved atomic (S⁰) and segregated cluster (Sn²⁻) forms ($\approx 30\text{--}40\ \text{at.}\ \%$) in
86 the nanocrystalline surface layer (Figs. 1a,b).

87 Detailed imaging and structural characterization of the layer cross-section were performed
88 by means of transmission electron microscopy (TEM, accelerating voltage – 200 kV, point-to-
89 point resolution – 0.19 nm) using JEOL JEM-2100F equipped by an energy-dispersion x-ray
90 spectroscopy (EDX) module. Cross-sectional specimens for TEM were prepared in a common
91 way, involving mechanical grinding and subsequent thinning of a sample by Ar⁺ ion milling
92 at 4 keV ion energy. Selected area electron diffraction (SAED) patterns were obtained using a
93 100-nm selective aperture. Elemental maps were acquired in a scanning (STEM) mode, using
94 1-nm spot size for enhanced spectrum collection rates.

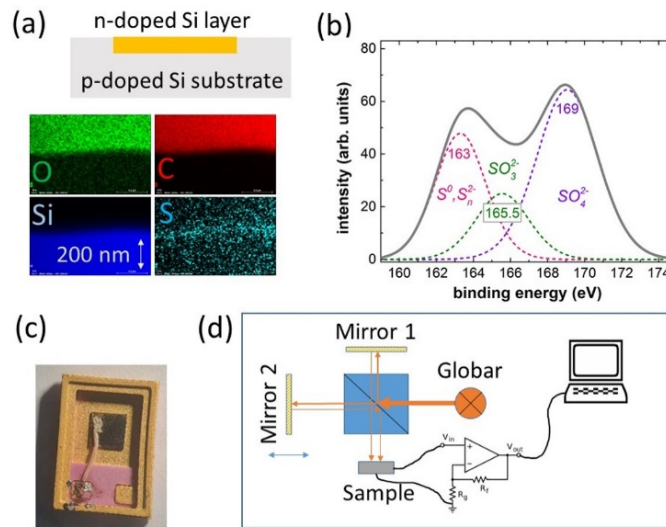


Fig. 1. (a) Functional layout of the n-p junction made by n-hyperdoped layer on the p-doped Si substrate and corresponding EDX elemental maps (prior ultrasonic cleaning). (b) XPS spectrum of S_{2p} -band of sulfur, its deconvolution and assignment after [31]. (c) image of the PC element. (d) IR-PC acquisition arrangement: globar, KBr splitter, sample, electrical scheme, Bruker spectrometer.

95 During fabrication of the photoconductive (PC) element, the sulfur-hyperdoped/annealed
 96 sample was mounted into a diode case (Fig. 1c), where back and front electrodes were 100-nm
 97 thick gold films, deposited via magnetron sputtering. The back (substrate) side of the sample
 98 was fully covered by gold to provide the large contact area. The laser-treated front side was partially
 99 covered by the metal layer. Rear and front electrical contracts were glued with silver paste. In
 100 this way, a PC sample with a vertical arrangement and large photosensitive contact area equal to
 101 $5 \times 5 \text{ mm}^2$ was obtained. Relatively high conductivity of the sulfur-hyperdoped layer provided
 102 good lateral current distribution.

103 Mid-IR photoconductivity experiment was carried out using a Bruker IFS 125 HR all-range
 104 high-resolution vacuum Fourier spectrometer (Fig. 1d). A Cryomech PT 403 closed-cycle
 105 helium cryostat was used for sample cooling in the temperature range of 5-300 K, controlling
 106 the temperature by means of a Lakeshore 335 controller and a silicon sensor. A KBr optical
 107 window was used as the entrance window of the cryostat. As a radiation source was used a
 108 globar with a KBr beam-splitter. To register the photoconductivity in the spectral range of 2-25
 109 μm , a self-made electronic circuit with a preamplifier was used, the signal from which was fed
 110 by the analog output of the spectrometer. The PC spectra were obtained with different voltage
 111 biases in the range from -10 V to +10 V, indicating no dependence of the PC spectra on the
 112 voltage value or sign. To correct the signal on the blackbody emission, as well as to take into
 113 account various spectral features of the optical components of the spectrometer, measurements
 114 were carried out with similar optical components and parameters, where the DLaTGS linear
 115 pyroelectric detector served as a radiation detector. The sulfur-hyperdoped/annealed mounted
 116 sample was tested by IR-PC spectroscopy in the temperature range of 5-105 K, blocking/splitting
 117 the visible part of incident light by a KBr splitter. To prevent distortion of the photoconduction
 118 signal due to non-linear responses, the following checks were performed. First, we checked the
 119 shape of the signal when the sample was irradiated with different intensities of light. Second, the
 120 signal was investigated at different rates of modulation of radiation by a Fourier spectrometer

121 (from 1 to 30 kHz). Once nonlinear processes depend on time and intensity, these check would
122 allow us to evaluate the possible nonlinear distortion of the signal. However, we did not observe
123 any noticeable changes in the spectra.

124 **3. Results and discussion**

125 *3.1. Broadband (2-21 μm) structured photoconductivity of liquid-helium cooled hyper-* 126 *doped Si: spectral assignment of sulfur centers*

127 The typical acquired broad-range (60-500 meV, 2.4-20.8 μm , 480-4200 cm^{-1}) PC spectrum
128 of the hyperdoped Si is shown in Figure 2, where the accessory rocking (450 cm^{-1}), bending
129 (800 cm^{-1}) and stretching (1075 cm^{-1}) Si-O-Si bands and other contaminants are absent [32].
130 Comparing to room-temperature broad and continuous near-mid-IR absorption spectra of weaker
131 hyperdoped Si samples in the most of previous studies (see the bibliography in [9–13]) due to the
132 deep cooling this spectrum demonstrates a number of well-resolved spectral bands, which can be
133 readily assigned as follows [25–27]. Besides the common mid-IR bands of atomic-like S^+ and S^0
134 centers (ground-state binding energy $E_{\text{S}^+} = 614$ meV, $E_{\text{S}^0} = 318$ meV) [25], the interesting feature
135 in Figure 2 is the set of rather strong and well-resolved spectral bands in the range $\lambda \approx 5\text{-}20$ μm .
136 These bands apparently indicate the rarely observed, usually very weak absorption of S-clusters
137 S_2^0 , S_2^+ , $\text{S}_c^0(\text{X}_{1-5})$ and $\text{S}_c^+(\text{X}_1)$, as well as absorption of the anticipated similar centers $\text{S}_c^+(\text{X}_{2-5})$,
138 which are, by the analogy with S_2^+ and $\text{S}_c^+(\text{X}_1)$, two-fold higher energy (the overall binding energy
139 range $\approx 50\text{-}250$ meV) [25–27]. Here, these PC band can be observed in mid-far IR PC spectra
140 due to the liquid-helium cooling and high abundance of the highly aggregated cluster forms
141 of sulfur atoms. In its turn, such high atomic aggregation became possible due to the high
142 overall concentration of sulfur impurity in the n-doped surface layer, including also accessory
143 sulfur sediments on the surface and nanograin boundaries, which could be minimized, e.g., by
144 dissolution upon high-temperature (>1100 $^\circ\text{C}$) [14–17] annealing.

145 Hence, at the liquid-helium temperatures, preventing bleaching of shallow states of highly-
146 aggregated charged and neutral sulfur-donor centers via their thermal ionization and electron-
147 phonon scattering, broad near-far IR photoconductivity spectrum of the hyperdoped Si demon-
148 strates a large set of their corresponding spectral bands. The observed extraordinary extension of
149 the spectral photoconductivity response toward far-IR was assigned, first, to high dopant concen-
150 tration, providing near-far-IR absorbing highly-aggregated of sulfur cluster centers [13, 17, 28, 29].
151 Other driving factors are dopant annealing conditions [14–17], and the low operation temperatures,
152 as shown below.

153 *3.2. Temperature effects in mid-IR photoconductivity of hyperdoped Si: quantum-level* 154 *damping via electron-phonon interaction in different sulfur aggregation states*

155 Temperature effects on photoconductivity of the hyperdoped Si were studied in the range of 5-105
156 K for the most intense part of its mid-IR PC spectrum presented in Fig. 2 (Fig. 3, wavenumbers
157 $\nu = 1200\text{-}8000$ cm^{-1} , $\lambda \approx 1.25 - 8.3$ μm). The influence of temperature is expected to damp
158 and broaden these present spectral bands with interactions of the corresponding shallow donor
159 electronic states with thermally-excited low-energy lattice phonons [33] and their depopulation
160 via thermal ionization [34].

161 Indeed, in Fig. 3 a strong decrease in the PC spectral intensity is observed versus the increasing
162 temperature, starting at the lower temperatures $T < 35$ K in the low-wavenumber range and
163 then extending to the high-wavenumber range at higher temperatures $T > 85$ K. Specifically,
164 one can highlight two main trends in the temperature dependence of the PC bands: 1) the total
165 drop at the lower temperatures $T < 35$ K till the noise level for the low-wavenumber centers S_2^0 ,
166 $\text{S}_c^+(\text{X}_3)$, the simultaneous partial drop for the medium-wavenumber centers $\text{S}_c^+(\text{X}_{1,2})$, S_2^+ and the
167 subsequent persistence at this level till ≈ 85 K; 2) the final drop to the noise level for all these

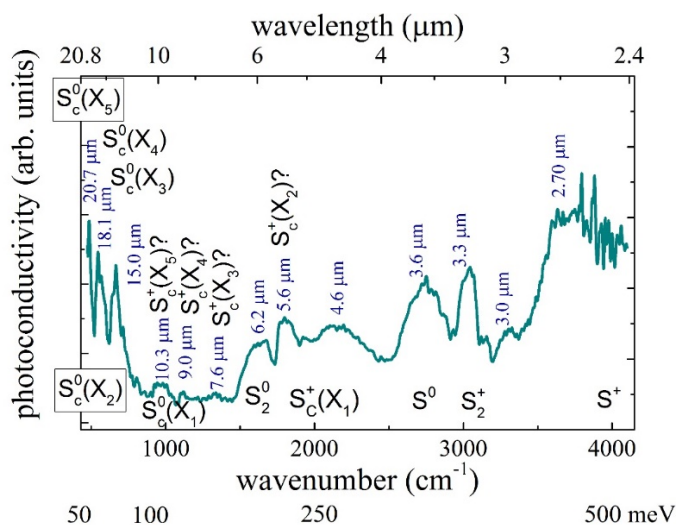


Fig. 2. PC spectrum of the photoelement at 5K-temperature with spectral assignment of the spectral bands after [25–27]. The anticipated spectral positions of unknown centers $S_c^+(X_{2-5})$, which could be twice higher in energy regarding the position of corresponding neutral centers, are shown with the question mark.

168 centers $S_c^+(X_{1,2})$, S_2^+ and even high-wavenumber centers S^0 , S^+ . These trends are overviewed in
 169 Fig. 4a as a function of temperature.

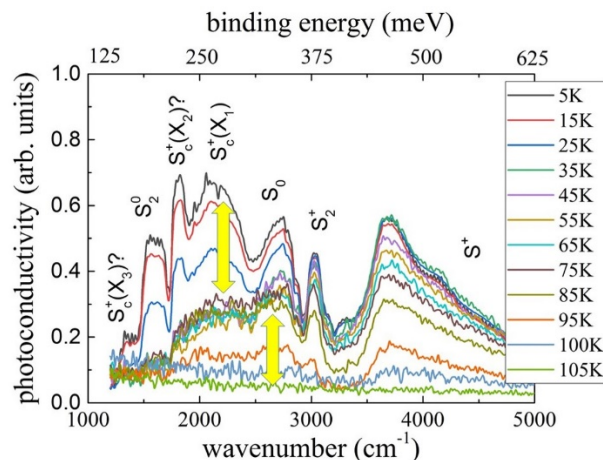


Fig. 3. Color PC spectra of hyperdoped Si at different temperatures in the range of 5-105 K with the spectral assignment after [25–27]. The yellow bilateral arrows indicate the lower-temperature (< 35 K, upper arrow) and higher-temperature (> 85 K, bottom arrow) ranges of PC damping, with the anticipated spectral positions of unknown centers $S_c^+(X_{2-5})$ shown with the question mark.

170 In a fair assumption that the observed thermally-induced changes in the photoelectrical
 171 properties of the hyperdoped Si are barrier-like processes with certain center-specific activation
 172 energies ε_i , the PC intensities were presented in $\ln\Phi_i - 1/T$ coordinates and linearly fitted to
 173 evaluate these magnitudes ε_i (Fig. 4b). The derived activation energies demonstrate two

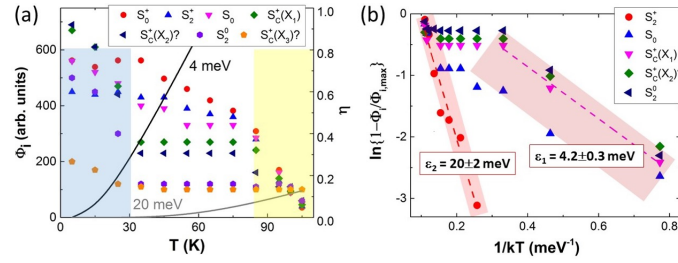


Fig. 4. (a) PC spectral intensity Φ_i for the different sulfur-donor centers versus T (left axis), right axis - phonon occupation numbers at $\varepsilon_1 \approx 4$ meV and $\varepsilon_2 \approx 20$ meV). (b) Dependences $\ln\{1-\Phi_i/\Phi_{i,max}\}$ - $1/kT$ with their linear fitting curves and activation energies ε_i as the linear slopes (b).

174 characteristic values $\varepsilon_1 = 4.2 \pm 0.3$ meV and $\varepsilon_2 = 20 \pm 2$ meV, effective in the temperatures ranges
 175 < 35 K ($kT < 3$ meV) and > 85 K ($kT > 7$ meV), respectively, while are still much lower, than the
 176 electron binding energies of the centers $E \approx 50$ -600 meV, and comparable to the corresponding
 177 values kT (Fig. 3). Therefore, one should look at other sulfur-related lower-energy excitations in
 178 the material, e.g., intra-center phonons and local vibrational modes.

179 Particularly, the activation energy $\varepsilon_1 \approx 4$ meV could be directly related to the lowest energy
 180 phonon ($\hbar\Omega_{min} \approx 4$ meV) in a crystalline lattice of face-centered orthorhombic sulfur unit cell
 181 (space group D_{2h}^{24} (Fddd) [35], which has the population factor [36]

$$\eta(\hbar\Omega_{min}, T) = \frac{1}{\exp(\hbar\Omega_{min}/kT) - 1}, \quad (1)$$

182 becoming considerable in the temperature range < 35 K (Fig. 4a), once the high phonon-mode
 183 degeneracy is accounted [35]. Such phonons could exist in nanocrystalline sulfur sediments,
 184 as revealed by our XPS characterization (Fig. 1b), which are resided on the Si crystallite
 185 boundaries in the nanocrystalline hyperdoped Si, providing its mid-IR PC response (Fig. 3).
 186 Such sediments may unavoidably appear during high-temperature stationary annealing and the
 187 following rapid quenching of the hyperdoped Si samples [14–17]. Thermal population of the
 188 Raman-active phonon mode induces the PC damping via strong electron-phonon scattering in
 189 the sulfur nanocrystallites [33].

190 In contrast, at higher temperatures > 85 K much higher activation energy ≈ 20 meV comes
 191 into play in the PC response (Figs. 3,4). Again, its magnitude is much lower, than the electron
 192 binding energies of the centers $E \approx 50$ -600 meV [25–27], or even zone-edge phonon energies
 193 in crystalline Si (12-16 and 55-63 meV for the acoustic and optical modes, respectively) [37].
 194 Meanwhile, it is still related to the same PC spectral bands in Fig. 3, indicating close relation to
 195 their underlying sulfur centers. Specifically, one can relate this five-fold higher activation energy
 196 to the lowest energy of Raman-active vibrations $\nu_8(e_2)$ of sulfur molecular octagons ($\hbar\Omega_{mean} \approx$
 197 20 meV) in the orthorhombic crystalline sulfur [35]. Moreover, according to Fig. 4b, such
 198 molecular-like sulfur vibrations could be also related to substitutional S-ion in the S^+ , S_2^+ -centers
 199 or S-atom in S^0 -center, and to sulfur atoms bound to surrounding Si atoms, since vibrational
 200 spectroscopy of sulfur impurity in Si is not well explored yet.

201 Overall, the unexpectedly strong effect of the limited (5-35 or 85-105 K) temperature variation
 202 on the spectrally-resolved photoconductivity characteristics of the sulfur-donor hyper-doped Si
 203 was observed. Its detailed characterization in terms of thermal activation energies indicates
 204 that quantum-level, single-particle thermal excitation of the lowest-energy phonon modes in
 205 the embedded sulfur nanocrystallites is underlying the observed two-step de-activation of the
 206 IR-photoconductivity through electron-phonon scattering. More enlightening and detailed picture

207 of broader IR-THz-range spectral (1-1000 μm) PC response and related temperature effects for a
208 large number of samples with variable abundance of different sulfur-donor centers is in progress
209 and will be presented in our forthcoming publications.

210 4. Conclusions

211 Crystalline, moderately p-doped silicon wafer, strongly laser-hyperdoped in its sub-micrometer
212 surface layer by donor sulfur, demonstrates very broad near-far IR (2-21 μm) photoconductivity
213 spectra of its donor centers in different charge and sulfur aggregation states, well-resolved
214 at the liquid-helium temperatures. At higher temperatures in the range of 5-105 K, two-step
215 de-activation of the photoconductivity response occurs via electron-phonon scattering due to
216 thermal population of the lowest-energy sulfur lattice phonon (<35 K) and the related lowest-
217 energy molecular-like sulfur vibration mode (85-105 K). The minimal temperature variation in
218 the ranges of 5-35 and 85-105 K, providing the strong PC damping, indicates its efficient and
219 spectrally-specific temperature control in the hyperdoped Si for potential broad-IR and even THz
220 applications.

221 **Acknowledgments.** Russian Foundation for Basic Research (18-29-20022).

222 **Disclosures.** The authors declare no conflicts of interest.

223 **Data availability.** Data underlying the results presented in this paper are available from the authors upon
224 reasonable request.

225 References

- 226 1. I. Gayduchenko, S. G. Xu, G. Alymov, M. Moskotin, I. Tretyakov, T. Taniguchi, K. Watanabe, G. Goltsman, A. K.
227 Geim, G. Fedorov, D. Svintsov, and D. A. Bandurin, "Tunnel field-effect transistors for sensitive terahertz detection,"
228 *Nat. Commun.* **12**, 2041–1723 (2021).
- 229 2. Q. Qiu and Z. Huang, "Photodetectors of 2d materials from ultraviolet to terahertz waves," *Adv. Mater.* **33**, 2008126
230 (2021).
- 231 3. S. Adachi, *Optical Properties of Crystalline and Amorphous Semiconductors* (Springer, Boston, MA, 1999).
- 232 4. H. Ferhati, F. Djeflal, A. Saidi, A. Benhaya, and A. Bendjerad, "Effects of annealing process on the structural and
233 photodetection properties of new thin-film solar-blind uv sensor based on si-photonics technology," *Mater. Sci.*
234 *Semicond. Process.* **121**, 105331 (2021).
- 235 5. J.-M. Pouirol, C. Majorel, N. Chery, C. Girard, P. R. Wiecha, N. Mallet, R. Monflier, G. Larrieu, F. Cristiano, A.-S.
236 Royet, P. A. Alba, S. Kerdiles, V. Paillard, and C. Bonafos, "Hyper-doped silicon nanoantennas and metasurfaces for
237 tunable infrared plasmonics," *ACS Photonics* **8**, 1393–1399 (2021).
- 238 6. E. D. Palik, *Handbook of optical constants of solids*, vol. 3 (Academic Press, 1997).
- 239 7. M.-J. Sher and E. Mazur, "Intermediate band conduction in femtosecond-laser hyperdoped silicon," *Appl. Phys. Lett.*
240 **105**, 032103–032103 (2014).
- 241 8. S. Q. Lim, A. J. Akey, E. Napolitani, P. K. Chow, J. M. Warrender, and J. S. Williams, "A critical evaluation of ag-
242 and ti-hyperdoped si for si-based infrared light detection," *J. Appl. Phys.* **129**, 065701 (2021).
- 243 9. C. Crouch, J. Carey, M. Shen, E. Mazur, and F. Génin, "Infrared absorption by sulfur-doped silicon formed by
244 femtosecond laser irradiation," *Appl. Phys. A* **79**, 1635–1641 (2004).
- 245 10. M. Aziz, T. Kim, and J. Warrender, "Strong sub-band-gap infrared absorption in silicon supersaturated with sulfur,"
246 *Appl. Phys. Lett.* **88**, 241902 (2006).
- 247 11. I. Umezu, J. Warrender, S. Charnvanichborikarn, A. Kohno, J. Williams, M. Tabbal, D. Papazoglou, X.-C. Zhang,
248 and M. Aziz, "Emergence of very broad infrared absorption band by hyperdoping of silicon with chalcogens," *J.*
249 *Appl. Phys.* **113**, 213501 (2013).
- 250 12. K.-M. Guenther, T. Gimpel, J. Tomm, S. Winter, A. Ruibys, S. Kontermann, and W. Schade, "Excess carrier
251 generation in femtosecond-laser processed sulfur doped silicon by means of sub-bandgap illumination," *Appl. Phys.*
252 *Lett.* **104**, 042107 (2014).
- 253 13. L. V. Nguen, S. I. Kudryashov, A. A. Rudenko, R. A. Khmel'nitsky, and A. A. Ionin, "Separation of mid-ir
254 light trapping and sulfur-donor absorption in nanosecond-laser sulfur-hyperdoped silicon: a way to spatially- and
255 spectrally-engineered interband ir-absorption," *J. Russ. Laser Res.* **39**, 192–199 (2018).
- 256 14. B. Newman, M.-J. Sher, E. Mazur, and T. Buonassisi, "Reactivation of sub-bandgap absorption in chalcogen-
257 hyperdoped silicon," *Appl. Phys. Lett. - APPL PHYS LETT* **98**, 1905–251905 (2011).
- 258 15. C. Wen, W. Chen, Y. Chen, K. Liu, X. Li, S. Hu, and Y. Yang, "Thermal annealing performance of sulfur-hyperdoped
259 black silicon fabricated using a nd:yag nanosecond-pulsed laser," *Mater. Res. Bull.* **93**, 238–244 (2017).
- 260 16. T. Gimpel, S. Winter, M. Boßmeyer, and W. Schade, "Quantum efficiency of femtosecond-laser sulfur hyperdoped
261 silicon solar cells after different annealing regimes," *Sol. Energy Mater. Sol. Cells* **180**, 168–172 (2018).

- 262 17. S. Kudryashov, L. Nguyen, D. Kirilenko, P. Brunkov, A. Rudenko, N. Busleev, A. Shakhmin, A. Semencha,
263 R. Khmel'nitskiy, N. Melnik, I. Saraeva, A. Nastulyavichus, A. Ionin, E. Tolordava, and Y. Romanova, "Large-scale
264 laser fabrication of anti-fouling si surface nanosheet arrays via nanoplasmonic ablative self-organization in liquid cs2
265 tracked by sulfur dopant," *ACS Appl. Nano Mater.* **1**, 2461–2468 (2018).
- 266 18. J. Carey, C. Crouch, M. Shen, and E. Mazur, "Visible and near-infrared responsivity of femtosecond-laser
267 microstructured silicon photodiodes," *Opt. letters* **30**, 1773–5 (2005).
- 268 19. P. Saring, A. L. Baumann, B. Schlieper-Ludewig, S. Kontermann, W. Schade, and M. Seibt, "Electronic and structural
269 properties of femtosecond laser sulfur hyperdoped silicon pn-junctions," *Appl. Phys. Lett.* **103**, 061904 (2013).
- 270 20. A. Said, D. Recht, J. Sullivan, J. Warrender, T. Buonassisi, P. Persans, and M. Aziz, "Extended infrared photoresponse
271 and gain in chalcogen-supersaturated silicon photodiodes," *Appl. Phys. Lett.* **99**, 073503–073503 (2011).
- 272 21. J.-H. Zhao, X.-B. Li, Q.-D. Chen, and H.-B. Sun, "Ultrafast laser induced black silicon, from micro-nanostructuring,
273 infrared absorption mechanism, to high performance detecting devices," *Mater. Today Nano* **11**, 100078 (2020).
- 274 22. X. Jin, Q. Wu, S. Huang, G. Deng, Y. Jianghong, H. Huang, P. Zhao, and J. Xu, "High-performance black silicon
275 photodetectors operating over a wide temperature range," *Opt. Mater.* **113**, 110874 (2021).
- 276 23. M. Wang, E. García-Hemme, Y. Berencén, R. Hübner, Y. Xie, L. Rebohle, C. Xu, H. Schneider, M. Helm, and
277 S. Zhou, "Silicon-based intermediate-band infrared photodetector realized by te hyperdoping," *Adv. Opt. Mater.* **9**,
278 2001546 (2021).
- 279 24. H. Jiang and C. Chen, "Analysis and calculation of electronic properties and light absorption of defective sulfur-doped
280 silicon and theoretical photoelectric conversion efficiency," *The J. Phys. Chem. A* **119**, 3753–3761 (2015).
- 281 25. H. Grimmeiss, E. Janzen, and B. Skarstam, "Deep sulfur-related centers in silicon," *J. Appl. Phys.* **51**, 4212–4217
282 (1980).
- 283 26. R. E. Peale, K. Muro, and A. J. Sievers, "Sulfur-hydrogen donor complexes in silicon," In *Mater. Sci. Forum* **65**,
284 151–156 (1991).
- 285 27. P. Wagner, C. Holm, E. Sirtl, R. Oeder, and W. Zulehner, "Chalcogens as point defects in silicon," in *In Advances in*
286 *Solid State Physics*, (Springer, Berlin, Heidelberg, 1984).
- 287 28. A. Ionin, S. Kudryashov, S. Makarov, N. Melnik, A. Rudenko, P. Saltuganov, L. Seleznev, D. Sinitsyn, I. Timkin,
288 and R. Khmel'nitskiy, "Structural and electrical characteristics of a hyperdoped silicon surface layer with deep donor
289 sulfur states," *JETP Lett.* **100**, 55–58 (2014).
- 290 29. S. Kudryashov, A. Nastulyavichus, D. Kirilenko, P. Brunkov, A. Shakhmin, A. Rudenko, N. Melnik, R. Khmel'nitskiy,
291 V. Martovitskii, M. Uspenskaya, D. Prikhodko, S. Tarelkin, A. Galkin, T. Drozdova, and A. Ionin, "Mid-ir-sensitive
292 n/p-junction fabricated on p-type si surface via ultrashort pulse laser n-type hyperdoping and high-temperature
293 annealing," *ACS Appl. Electron. Mater.* **3**, 769–777 (2021).
- 294 30. S. I. Kudryashov, A. A. Nastulyavichus, I. N. Saraeva, A. A. Rudenko, D. A. Zayarny, and A. A. Ionin, "Deeply
295 sub-wavelength laser nanopatterning of si surface in dielectric fluids: Manipulation by surface plasmon resonance,"
296 *Appl. Surf. Sci.* **519**, 146204 (2020).
- 297 31. C. D. Wagner, "Nist x-ray photoelectron spectroscopy database," NIST Standard Reference Database 20 (2020),
298 <https://srdata.nist.gov/xps/>.
- 299 32. M. T. Kim, "Deposition behavior of hexamethyldisiloxane films based on the ftir analysis of si–o–si and si–ch3 bonds,"
300 *Thin Solid Films* **311**, 157–163 (1997).
- 301 33. M. Cardona, "Electron-phonon interaction in tetrahedral semiconductors," *Solid State Commun.* **133**, 3–18 (2005).
- 302 34. K. Nakashima and M. Chijiwa, "Optical and thermal ionization of iron-related defects in silicon," *Jpn. J. Appl. Phys.*
303 **25**, 234–237 (1986).
- 304 35. A. Anderson and Y. Loh, "Low temperature raman spectrum of rhombic sulfur," *Can. J. Chem.* **47**, 879–884 (1969).
- 305 36. Y. U. Peter and M. Cardona, *Fundamentals of semiconductors: physics and materials properties* (Springer Science &
306 Business Media, 2010).
- 307 37. O. Madelung, ed., *Semiconductors—basic data* (Springer Science & Business Media, 2012).